Estimation of Precipitable Water for Improving Land Subsidence Accuracy Using DInSAR Technique

Naoya Maeda[1], Junichi Susaki[1] and Shin Akatsuka[2]
1: Kyoto University, C1-1-206, Kyotodaigaku-katsura, Nishikyo-ku, Kyoto, 615-8540, Japan,
Email: {maeda.naoya.24n, susaki.junichi.3r}@st.kyoto-u.ac.jp
2: Kochi University of Technology, B301, 185 Miyanokuchi, Tosayamada, Kami, Kochi, 782-8502, Japan,
Email: akatsuka.shin@kochi-tech.ac.jp

KEY WORDS: Precipitable water, Differential SAR interferometry, Atmospheric delay

ABSTRACT: Differential SAR interferometry (DInSAR) technique can quantitatively measure surface subsidence by using the phase difference at each pixel derived from multi-temporal SAR images. However, the phase difference contains several types of errors. Atmospheric delay is a major source of errors for surface subsidence estimation. In this study, we examined the availability of precipitable water (PW) as external data which indicates directly atmospheric state for the purpose of improving DInSAR. In the proposed method, we estimate spatially and temporally high resolution of PW, and calculate atmospheric delay at each pixel with estimated PW. The image of the atmospheric delay of each interferogram is acquired by taking a difference between the value of master image and that of slave image. This image indicates the state of atmosphere which changes by time and place, and we succeeded in making the image related to atmospheric error. In addition, we showed the possibility that we could remove the atmospheric error and improve accuracy of DInSAR by the proposed method.

1. INTRODUCTION

Excessive drawing ground water and natural gas brine causes surface subsidence, and as a consequence, building foundation may be damaged. In order to grasp this deformation, the method of correctly measuring extensive subsidence is needed to be developed. There is DInSAR which is one of the methods. However, the result of DInSAR contains several errors, e.g. atmospheric error, orbital error, and elevation error (Kampes, 2006).

Atmospheric delay mainly influences subsidence estimation. This error is caused by topography and horizontal inhomogeneity of water vapor distribution. Furthermore, the phase includes more this error when we apply this technique to the area where is humid and water vapor greatly changes as Japan. Therefore, we need to remove this error in order to estimate deformation correctly. There are a lot of researches related to removal of this error. Fujiwara et al. proposed that this error could be modeled as linear function of height (Fujiwara et al., 1999). However, this error includes the component depending on not only height but also heterogeneity of water vapor distribution. Thus, the structure of atmosphere is too complex to be modeled as a linear function of height.

In this study, we discuss the availability of precipitable water (PW) as external data which indicates directly atmospheric state. In the proposed method, we calculate the value of atmosphere delay and remove it from the phase of each interferogram after estimation of PW at each pixel. In existing researches related to PW estimation, Akatsuka et al. (2013) proposed two methods for estimating PW. First method uses brightness temperature observed by Multi-functional Transport Satellite (MTSAT), and it generates low accuracy of cloud mask and low resolution, e.g. 4 km spatial and 1 hour temporal resolution of the PW products. Second method uses digital elevation model (DEM) of Global 30 Arc-Second Elevation (GTOPO30) and re-analysis product of National Oceanic and Atmospheric Administration (NOAA), the United States of America. It also generates low resolution, e.g. 1 km spatial and 6 hour temporal resolution of the result. In this study, we estimate spatially and temporally high resolution of PW with utilizing 90m spatial resolution of DEM from Shuttle Radar Topography Mission (SRTM) and 1 hour temporal resolution of meteorological data which is a forecast value of a numerical meso scale model (MSM), e.g. surface temperature and surface pressure, provided by Research Institute for Sustainable Humanosphere, Kyoto University, Japan. We explain the PW and its role in Section 2, and we propose the method of calculating the delay along the slant range direction in order to apply to DInSAR in Section 3. We report the experimental results in Section 4 and discuss them in Section 5. Finally, we conclude this paper in Section 6.

2. THE ROLE OF PW AT THE TIME OF REMOVING THE INFLUENCE BY ATMOSPERIC DELAY

2.1 PW

PW is the total atmospheric water vapor contained in a vertical column of unit area from earth's surface to top of atmosphere. Recently, PW is noticed as meteorological data which indicates directly atmospheric state. Moreover, PW can be observed with radiosonde. More specifically, we can calculate PW using observed pressure and specific humidity (Equation (1)).

$$\mathrm{PW} = \frac{100}{g}\left[q_{0,1}(p_0 - p_1) + q_{1,2}(p_1 - p_2) + \cdots\right]. \tag{1}$$

Here, g is gravity acceleration, p_0 is surface pressure, p_i is pressure at *i*th altitude of observation and $q_{i,j}$ is the mean of specific humidity between p_i and p_j.

2.2 Relation of PW and the atmospheric delay

Atmospheric delay in the zenith direction (ΔL_{Zenith}) is calculated (Equation (9)).

$$\Delta L_{Zenith} = 10^{-6}\left[\int_{Zenith} k_1 \frac{R}{m_d}\rho dz + k_2' \int_{Zenith}\left(\frac{P_v}{T}\right) Z_v^{-1}\, dz + k_3 \int_{Zenith}\left(\frac{P_v}{T^2}\right) Z_v^{-1} dz\right]. \tag{2}$$
$$k_2' = \left(k_2 - k_1 \frac{m_v}{m_d}\right).$$

Here, T is surface temperature, P_v is partial pressure of water vapor, Z_v is the compression ratio of water vapor, k_1, k_2, k_3 are constant, m_d and m_v are the molecular weight of dry air and water vapor and R is gas constant.

Equation (2) can be divided into term 1 which is proportional to surface pressure and terms 2 and 3 which are proportional to both amounts of water vapor and temperature, resepectively. The term 1 is called as Zenith Hydrostatic Delay (ZHD). The term 2 and 3 are called as Zenith Wet Delay (ZWD). Because of ZHD's feature, ZHD depends on elevation. Therefore, the influence of ZHD in PSInSAR is small when we take a difference between two pixels whose coordinate and elevation are same at two different times in differential interferogram processing. On the other hand, ZWD largely changes between images because the distribution of water vapor greatly depends on time and place. In this study, we improve accuracy of interferogram by removing the error of ZWD. Besides, ZWD can be calculated by Equation (3) (Askne and Nordius, 1987).

$$\mathrm{ZWD} = 10^{-5} \times R_v \left[k_2' + \frac{k_3}{T_m}\right] \times \mathrm{PW}. \tag{3}$$

Here, R_v is a gas constant of water vapor and T_m is the mean weighted temperature of atmosphere.

3. PROPOSED METHOD

3.1 Estimation of PW

We estimate spatially and temporally high resolutions of PW with 90 m spatial resolution of DEM from SRTM and 1 hour temporal resolution of MSM GPV data provided by Research Institute for Sustainable Humanosphere, Kyoto University, Japan. GPV data contains several data at each equi-pressure surface, e.g. specific humidity (SH), surface temperature (T), surface pressure (P_S), sea level surface pressure (P_{SL}). These data also contain relative humidity (RH) at each equi-pressure surface whose pressure is from 300 hPa to 1000 hPa. These data have spatial resolution of 0.05°×0.065° at ground surface and 0.1°×0.125° at pressure surface and temporal resolution of 1 hour at ground surface and 3 hours at pressure surface.

PW is estimated at each pixel using DEM and GPV. Due to the difference between the resolution of GPV and DEM, we interpolate the resolution of GPV to that of DEM. In this subsection, we discuss only a grid G_{mn} at GPV and a pixel D_{ij} included by the grid at DEM. Besides, the number of pixel included by G_{mn} is *u*×*v*, and D_{ij} (*i=1,2,..,u;*

j=1,2,..,v) is one of the pixel included by G_{mn}.

First, surface pressure ($P_{D_{ij}}$hPa) of D_{ij} is estimated. If temperature lapse rate is 6.5 K/km, the elevation ($h_{G_{mn}}$ km) and sea level surface temperature ($T_{SL\_G_{mn}}$ K) can be calculated by the equation of state and hydrostatic equilibrium (Equations (4) and (5)).

$$h_{G_{mn}} = \frac{T_{SL\_G_{mn}}}{0.0065} \times \left\{1 - \left(\frac{P_{SL\_G_{mn}}}{P_{S\_G_{mn}}}\right)^{5.257}\right\}. \quad (4)$$

$$T_{SL\_G_{mn}} = T_{S\_G_{mn}} + 0.0065 \times h_{G_{mn}}. \quad (5)$$

$P_{D_{ij}}$ is expressed using $h_{G_{mn}}$and $T_{SL\_G_{mn}}$ (Equation (6)).

$$P_{D_{ij}} = P_{SL\_G_{mn}} \times \left(1 - \frac{0.0065 \times h_{D_{ij}}}{T_{SL\_G_{mn}}}\right)^{5.257}. \quad (6)$$

Then, we estimate specific humidity ($\mathrm{SH}_{D_{ij}}$). Water vapor pressure ($e_{D_{ij}}$ hPa) and surface pressure ($P_{D_{ij}}$) are needed in order to estimate $\mathrm{SH}_{D_{ij}}$. Saturated water vapor pressure ($e_{sat\_D_{ij}}$ hPa) is explained by Tetens's equation (Equation (7)).

$$e_{sat\_D_{ij}} = 6.1078 \times 10^{\left\{7.5T_{D_{ij}}/(T_{D_{ij}}+237.3)\right\}}. \quad (7)$$

$e_{D_{ij}}$ is calculated by Equation (8) since relative humidity (RH) can be represented using ratio of $e_{D_{ij}}$to $e_{sat\_D_{ij}}$.

$$e_{D_{ij}} = \left(\frac{\mathrm{RH}\_G_{mn}}{100}\right) \times e_{sat\_D_{ij}}. \quad (8)$$

At pixels whose $P_{D_{ij}}$ are over 1000 hPa, $\mathrm{SH}_{D_{ij}}$ is estimated using surface pressure and water vapor pressure (Equation (9)).

$$\mathrm{SH}_{D_{ij}} = \frac{0.622}{\left(\frac{P_{D_{ij}}}{e_{D_{ij}}}\right) - 0.378}. \quad (9)$$

Finally, PW is estimated using $P_{D_{ij}}$and $\mathrm{SH}_{D_{ij}}$. Assuming that $\mathrm{RH}_{D_{ij}}$ is same as relative humidity of surface ($\mathrm{RH}_{G_{mn}}$) if $P_{D_{ij}}$ is over 1000 hPa, $SH_{D_{ij}}$ is calculated by Equations (5) to (9). Furthermore, we assume that $\mathrm{SH}_{D_{ij}}$ is same as $\mathrm{SH}_{G_{mn}}$ which is the value of the nearest upper equi-pressure surface if $P_{D_{ij}}$ is under 1000 hPa. PW between ground surface and equi-pressure surface of 300 hPa is expressed by

・$P_{D_{ij}} > 1000$ hPa

$$\mathrm{PW}_{D_{ij}} = \frac{100}{g}\left[\frac{\mathrm{SH}_{D_{ij}}+\mathrm{SH}_{1000}}{2}\left(P_{D_{ij}} - P_{1000}\right) + \frac{\mathrm{SH}_{1000}+\mathrm{SH}_{975}}{2}(P_{1000} - P_{975}) + \cdots + \frac{\mathrm{SH}_{P400}+\mathrm{SH}_{P300}}{2}(P_{400} - P_{300})\right]. \quad (10)$$

・$P_{D_{ij}} < 1000$ hPa

$$\mathrm{PW}_{D_{ij}} = \frac{100}{g}\left[\mathrm{SH}_{P_1}(P_D - P_1) + \frac{\mathrm{SH}_{P_1} + \mathrm{SH}_{P_2}}{2}(P_1 - P_2) + \cdots + \frac{\mathrm{SH}_{P_{400}} + \mathrm{SH}_{P_{300}}}{2}(P_{400} - P_{300})\right]. \quad (11)$$
$$(P_2 < P_1 \leq P_D < P_{1000})$$

3.2 Estimation of ZWD'

PW estimated in Subsection 3.1 is the value in zenithal direction. Therefore, only ZWD in zenithal direction is estimated when the value is substituted in Equation (3). However, in order to remove the atmospheric error correctly, we should integrate the errors along the direction of the microwave propagation path. Hereafter, we refer to ZWD' the integrated ZWD along the slant range direction. In this subsection, we explain the method of estimating ZWD'. Figure 1 shows the flow chart of this procession, and Figure 2 shows conceptual scheme of the estimation.

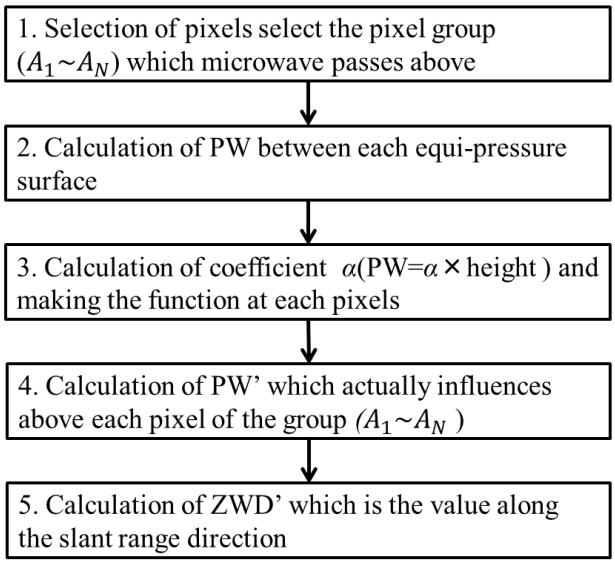

Figure 1. The flow chart of estimating ZWD'

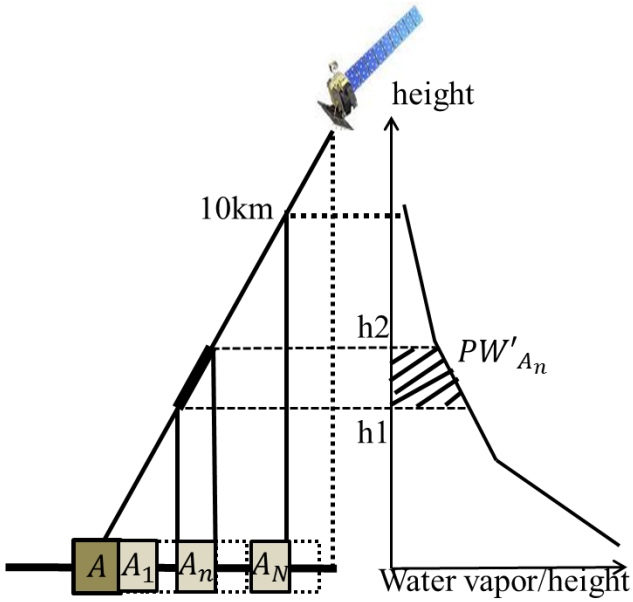

Figure 2. Conceptual scheme of the estimation

For simplicity, we discuss the calculation of one pixel (pixel *A*). In the step 1, we calculate the incident angle of pixel A with orbital information and select the pixel group (A_1~A_N) which microwave passes above at range direction. Then, only pixels whose altitude is less than 10 km are selected because most water vapor exists less than 10 km. The altitude is calculated with incident angle when microwave passed above each pixel of this group.

In the step 2, PW between ground surface and each equi-pressure surface (400-975 hPa) is estimated. These values can be acquired by the same method of estimating PW between ground surface and 300 hPa equi-pressure surface in Subsection 3.1. Moreover, PW between each equi-pressure surface ($\mathrm{PW}_{\mathrm{Dif}}$) is calculated by taking a difference between these values (Equation (12)).

$$\mathrm{PW}_{\mathrm{Dif}(1,2)} = \mathrm{PW}_1 - \mathrm{PW}_2. \quad (12)$$

Here, PW_i is PW between ground surface and *i*th equi-pressure surface.

In the step 3, we estimate coefficient (α) between each equi-pressure surface using $\mathrm{PW}_{\mathrm{Dif}}$ and the altitude difference (Δd). Thus, the vertical PW can be expressed as the function of altitude at each pixel (Equation (13)).

$$\mathrm{PW}_{\mathrm{Dif}} = \alpha \times \Delta d. \quad (13)$$

In the step 4, PW' actually influences ZWD' above each pixel of the group (A_1~A_N). The altitude change above

each pixel is calculated with incident angle and spatial resolution. Furthermore, PW′ is calculated with the function between equi-pressure surface including h_1 and h_2 (Equation (14)).

$$\mathrm{PW'}_{A_n} = \alpha\left(h_{n,2} - h_{n,1}\right). \tag{14}$$

If h_1 and h_2 exist different equi-pressure surface interval, PW' is calculated in Equation (15).

$$\mathrm{PW'}_{A_n} = \alpha_a\left(h_{n,2} - h_{n,3}\right) + \alpha_b\left(h_{n,3} - h_{n,1}\right). \tag{15}$$

Here, h_3 is the height of boundary between equi-pressure surfaces and α_i is coefficient of *i*th equi-pressure surface interval.

$\mathrm{PW'}_{\mathrm{A}}$ is the value along the slant range direction and can be estimated by summing up PW′ of this group (A_1~A_N) (Equation (16)).

$$\mathrm{PW'}_{\mathrm{A}} = \sum_{n=1}^{N} \mathrm{PW}'_{A_n}. \tag{16}$$

In the step 5, we substitute PW' into PW in Equation (3) in order to calculate ZWD' (Equation (17)).

$$\mathrm{ZWD}_{\mathrm{A}}' = 10^{-5} \times R_v \left[k_2' + \frac{k_3}{T_m}\right] \times \mathrm{PW}_{\mathrm{A}}'. \tag{17}$$

ΔZWD' of interferogram is acquired by taking the difference between ZWD' of master image and slave image observed at t_1 and t_2 (Equation (18)).

$$\Delta\mathrm{ZWD}'(t_1, t_2) = \mathrm{ZWD}'(t_1) - \mathrm{ZWD}'(t_2). \tag{18}$$

4. EXPERIMENT

4.1 Data used

We used 2 SAR images observed with ALOS-PALSAR as the Chiba data, Japan. Figure 4 shows the study area. HH-polarized master image and slave images were observed in an FBS mode on September 23, 2006 and December 24, 2006. The resolution of these images after multi-looking is 25 m in both directions of slant range and azimuth. To estimate ΔZWD', we used the GPV and DEM.

4.2 Results

The interferogram is shown in Figure.4 and the image of ΔZWD' shown in Figure 5. In addition, we show the phase value in Figure 6. We selected the pixels which contain permanent scatterers (PS) that are coherent over several years and make the pair of neighboring pixels and develop the network as triangulated irregular network (TIN). Thus, the phase difference between two neighboring pixels in both images is shown in the same way.

Figure 3. The area of SAR image
(red frame: the area of original SAR image write frame: experiment area)

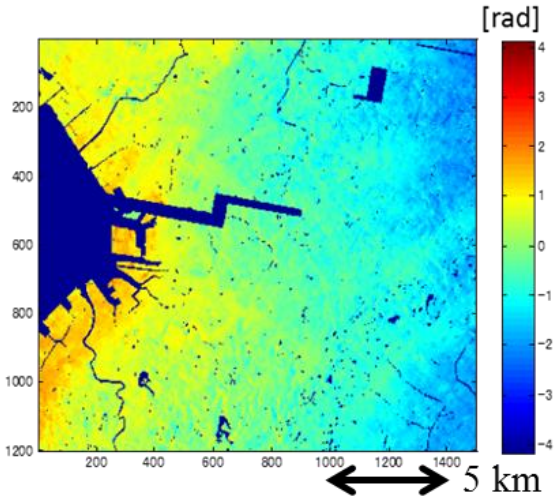

Figure 4. Interferogram
(master:2006/9/23 slave:2006/12/24)

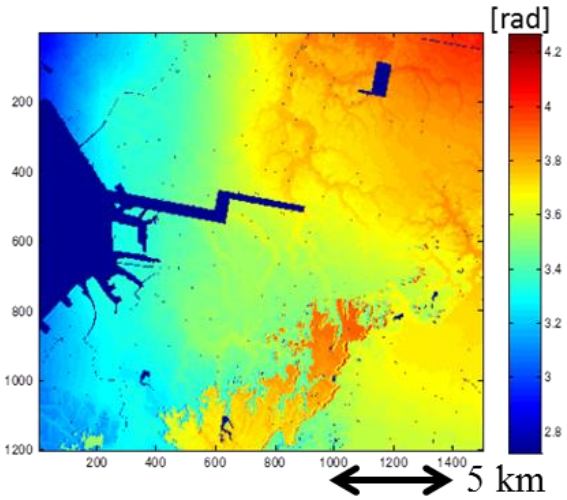

Figure 5. ΔZWD' image
(master:2006/9/23 slave:2006/12/24)

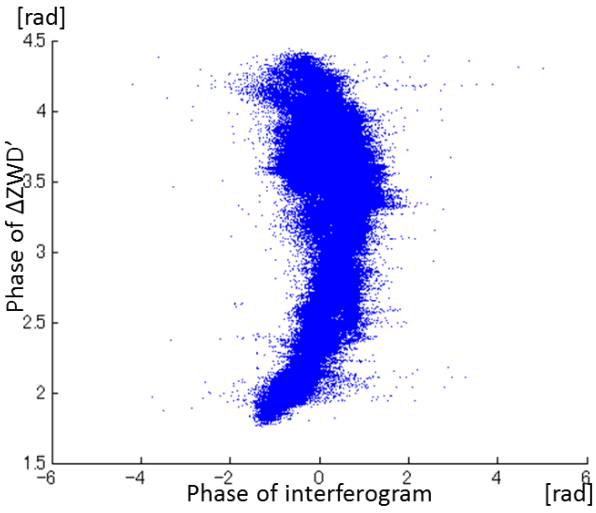

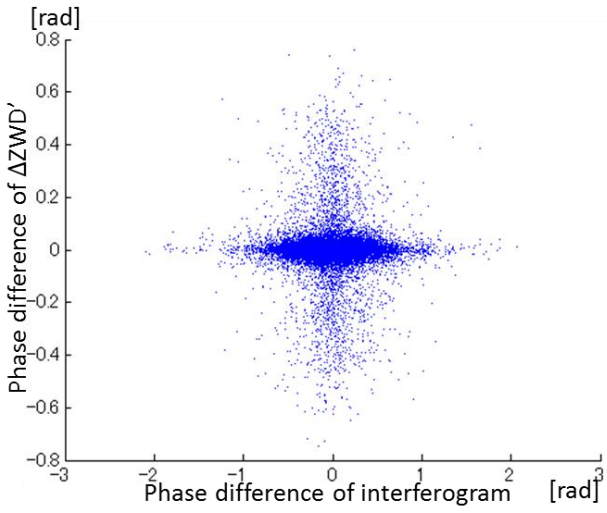

Figure 6. The scatter diagram of the phase of the interferogram and ΔZWD'

5. DISCUSSION

Figure 6 indicates that variation width of ΔZWD' was approximately 3 rad. And ΔZWD' has spatial correlation and is spatially smooth same as DEM and GPV. Moreover, ΔZWD' contains the component depending on elevation. The value of ΔZWD' changes by time since it is estimated with GPV which changes similarly. Thus, we could remove the atmospheric error more correctly by utilizing ΔZWD' than modeling this error as linear function of height. However, some error of ΔZWD' are removed in correction of range migration which is one of synthetic aperture processing. If we remove this error by utilizing estimated ΔZWD', this error is removed excessively. Therefore, ΔZWD' cannot be subtracted directly from interferogram. We examine the relation between phase of interferogram and ΔZWD', the relation between phase difference of both images. As a result, we could not confirm the correlation of two values in both cases. In this experiment, the data observed with L band radar is used. In the case of L band radar, the influence of ionosphere delay is large. Because of this, we might not confirm the correlation. Accordingly, we need to examine the correct process about ΔZWD' in order to apply to DInSAR.

6. CONCLUSIONS

We succeeded in estimation of PW whose spatial and temporal resolutions are high and calculation of ΔZWD'. Figure 5 shows that the atmospheric error changes by time and space. It may be possible that we can improve the accuracy of DInSAR by utilizing ΔZWD'. However, we must examine the technique of applying ΔZWD' to DInSAR because this value cannot be used directly. Furthermore, it is necessary to examine the application in other bands as a future problem. In this experiment, the data measured with L band radar was used. However, in the case of L band radar, the delay related to water vapor is relatively small. Therefore, we need to experiment with the data measured using C band radar influenced largely by water vapor. With the experiment, we confirm the correlation of the phase of interferogram and ΔZWD' and develop the method of utilizing ΔZWD'.

8. REFERENCES

Akatsuka, S., Oyoshi, K., and Takeuchi, W., 2013. Development of an Optimum Water Vapor Product for Land SurfaceTemperature Retrieval from MTSAT data. Journal of The Remote Sensing Society of Japan, 33(3), pp. 173-184.

Askne, J., and Nordius, J., 1987, Estimation of tropospheric delay for microwaves from surface weather data, Radio Science, 22, 379-386.

Ferretti, A., Prati, C., and Rocca, F., 2002. Nonlinear subsidence rate estimation using permanent scatterers in differential SAR interferometry. IEEE Transactions on Geoscience and Remote Sensing, 38(5), pp. 2202-2212.

Fujiwara, S., Tobita, M., Murakami, M., Nakagawa, H., and Rosen, P., A., 1999. Baseline Determination and Correction of Atmospheric Delay Induced by Topography of SAR Interferometry for Precise Surface Change Detection. Journal of the Geodetic Society of Japan, 45(4), pp. 315-325.

Kampes, M., B., 2006, Radar Interferometry, Springer Netherlands, pp. 5-30.

Ohtani, R., Tsuji, H., Mannoji, N., Segawa, J. and Naito, I., 1997. Precipitable Water Vapor Observed by Geographical Survey Institute's GPS Network. Meteorological Society of Japan, Tenki 44(5), pp. 317-325.